



Cite this: DOI: 10.1039/d5tc01738f

A multi-scale interface-induced 3D percolation network in polymeric heterostructures for EMI shielding application†

Jiahao Sun,^a Lijian Mao,^a Zhenliang Gao,^a Lechun Deng,^b Qiang Chen,^b Yang Li,^{*a} Chuntai Liu,^{ib} Changyu Shen^a and Xianhu Liu^{ib} ^{*a}

For addressing the limitations of traditional metal-based electromagnetic interference (EMI) shielding materials, such as insufficient flexibility and susceptibility to corrosion, this study developed a fluoro-silicone rubber (FVMQ) matrix composite with superior polarization response by constructing multi-scale heterogeneous interface structures. Multi-walled carbon nanotubes (MWCNTs) and silver-coated copper powder (Ag@Cu) were employed as functional fillers to optimize the electromagnetic and mechanical properties of the material system through precise regulation of the filler–matrix interface interactions. The metal–insulator interface formed between the Ag@Cu filler and the rubber matrix induces a strong interfacial polarization effect, thereby significantly enhancing the dielectric loss capacity of the material. Simultaneously, the three-dimensional network structure of MWCNTs not only improves the continuity of the conductive pathways but also markedly increases the crosslinking density of the composite due to its robust interaction with the rubber molecular chains. This multi-scale interface engineering effectively suppresses the formation of internal defects within the material, blocks water diffusion pathways, and enables the material to exhibit excellent corrosion resistance (contact angle >112°) and long-term stability. The results demonstrate that the heterogeneous composite possesses remarkable advantages in EMI shielding performance, achieving a shielding efficiency exceeding 109 dB. Notably, the material also exhibits superior electrothermal response characteristics under electrical stimulation. It can achieve rapid temperature elevation above 130 °C under a low-voltage drive of 3.5 V, while retaining outstanding mechanical properties (elongation at break >400% and tensile strength >3 MPa). The integration of EMI shielding, electrothermal conversion, and mechanical flexibility into a single multifunctional system highlights its potential for applications in complex environments. This study provides a critical interface design strategy for the development of next-generation flexible EMI shielding materials.

Received 30th April 2025,
Accepted 17th June 2025

DOI: 10.1039/d5tc01738f

rsc.li/materials-c

1. Introduction

In the context of rapid advancement of 5G/6G communication and smart wearable devices, the control of electromagnetic (EM) pollution presents significant challenges. Traditional metal-based materials suffer from inherent drawbacks such as high density and limited flexibility.^{1–5} In contrast, polymer-based composites have emerged as a research focus due to their strong designability and superior processability. Owing to their

unique molecular chain flexibility, rubber materials can be precisely fabricated using conventional compression molding or extrusion molding processes.^{6–9} This property renders them especially suitable for the fabrication of devices such as electromagnetic interference (EMI) shielding gaskets with specific structural requirements.^{10–13} Fluorosilicone rubber (FVMQ) is chosen as the base material, which not only retains the excellent processability of traditional rubber but also exhibits superior weather resistance and chemical stability.

Generally, the electrical conductivity of EMI shielding materials serves as a key indicator of their shielding performance. High-conductivity metals such as silver (Ag), copper (Cu), aluminum (Al), iron (Fe), and nickel (Ni) are incorporated into polymer matrices to enhance both the electrical conductivity and mechanical properties of the resulting composite material.^{14–18} Although Ag exhibits the highest conductivity

^a National Engineering Research Center for Advanced Polymer Processing Technology, Zhengzhou University, Zhengzhou, 450002, China.

E-mail: xianhu.liu@zzu.edu.cn

^b State Key Laboratory of Solidification Processing, School of Materials Science and Engineering, Northwestern Polytechnical University, 710072, Xi'an, China

† Electronic supplementary information (ESI) available. See DOI: <https://doi.org/10.1039/d5tc01738f>

among these metals, its prohibitively high cost limits its practical application as a conductive filler. Cu is an alternative option for improving the conductivity of polymers, with its electrical conductivity being only slightly lower than that of Ag.¹⁹ By utilizing Ag@Cu powder as a conductive filler, a layer of Ag with adjustable thickness can be deposited on the surface of Cu particles. This approach not only reduces the susceptibility of Cu powder to oxidation but also alleviates the issues of high cost and migration associated with pure Ag powder, thereby providing an ideal balance between high performance and cost-effectiveness.^{20–22}

In pursuit of lightweight, low-cost, and high-performance materials, researchers have achieved significant advancements in enhancing EMI shielding efficiency (EMI SE) by incorporating carbon materials (*e.g.*, carbon fibers and carbon nanotubes) and combining them with metallic fillers.^{23–25} For instance, Chen²⁶ *et al.* modified activated carbon fibers (CFs) with polydopamine (PDA), leveraging its self-polymerization properties to enhance the surface activity of the fibers. Subsequently, a uniform silver layer was chemically deposited onto the CFs *via* a silver-plating process, leading to the development of a flexible silver-coated carbon fiber/silicone rubber composite material with superior EM shielding capabilities. Chen²⁷ *et al.* innovatively designed a double-layer structure silicone rubber composite. Initially, an SiO₂ insulating layer was coated on the surface of carbonyl iron particles to form carbonyl iron@SiO₂ (CS) particles. Magnetic Ni@Ag (NA) particles were further introduced and magnetically assembled with the CS layer, resulting in the preparation of multistage-structured CSNA composite films that enable coordinated regulation of multiple EM wave loss mechanisms. Seoyoung *et al.*²⁸ developed a flexible and stretchable conductive composite material by blending micrometer-sized silver flakes (Ag flakes) with nano-silver-modified multi-walled carbon nanotubes (nAg-MWCNTs) into a nitrile butadiene rubber (NBR) matrix. The study demonstrated that the incorporation of nAg-MWCNTs not only significantly enhanced the conductivity of the composite through the construction of a three-dimensional conductive network but also increased interfacial polarization losses due to their unique nanostructure, thereby improving the shielding efficiency of the material in the X-band (8.2–12.4 GHz) by over 40%. This “micron–nano” collaborative enhancement strategy offers a novel approach for the development of high-performance flexible shielding materials.^{29,30} Nevertheless, critical challenges persist in current research. Most high-performance EMI shielding materials rely on metallic fillers such as silver and nickel, which, despite their excellent electrical conductivity, are prone to oxidation or electrochemical corrosion in corrosive environments like damp heat and salt spray, leading to a decline in shielding performance.^{31,32} For example, silver forms an insulating Ag₂S layer in sulfur-containing environments, while nickel develops an Ni(OH)₂ passivation layer under wet conditions, both of which substantially reduce the long-term stability of the materials. Although some studies have improved corrosion resistance through surface coating (*e.g.*, SiO₂ insulation layers) or alloying (*e.g.*, Ni@Ag core-shell structures), systematic

investigations into corrosion mechanisms for complex service environments remain insufficient.^{33–35} Furthermore, there is a lack of standardized accelerated aging tests and performance evaluation systems.

In this study, an innovative FVMQ-based composite with a “core-shell-net” heterogeneous structure was designed and fabricated. Core-shell Ag@Cu particles form an efficient polarization center at the metal–metal interface at the microscopic scale. MWCNTs were introduced to construct a three-dimensional percolation network at the mesoscopic scale. Their unique nanoconfinement effects significantly enhanced the interfacial polarization response. MWCNTs not only function as a conductive reinforcing phase but also form a dense cross-linked network structure through strong interactions with rubber molecular chains, effectively addressing the corrosion issue of metallic fillers. In terms of interface engineering, the local barrier formed by the interface between FVMQ molecular chains and heterogeneous fillers promotes space charge polarization. Furthermore, the hierarchical impedance matching structure constructed with multi-dimensional fillers realizes multiple scattering of EM waves. Accelerated aging tests demonstrated that the material exhibits excellent environmental stability under harsh conditions such as CASS (96 h), UV exposure (96 h), and mechanical bending (1000 bending cycles), with shielding efficiency decay remaining below 99.06%. Through multi-scale interface cooperative regulation, this study achieved an outstanding average EMI SE of 109 dB (X-band). This achievement not only overcomes the technical bottleneck of environmental durability in traditional composite materials but also provides critical theoretical guidance and a technical pathway for the development of advanced intelligent EM protection materials.

2. Experimental details

2.1. Materials

Fluorosilicone rubber (FVMQ) was purchased from Yuyao Jinchao Polymer Co., Ltd. The flake Cu powder (8–12 μm) was purchased from Nangong Xindun Alloy Welding and Spraying Co., Ltd. MWCNTs with a length of 10–30 μm and a diameter of 5–15 nm were purchased from TIMESNANO. AgNO₃, glucose (GS), anhydrous ethanol, and polyvinylpyrrolidone (PVP) were purchased from Sinopharm Chemical Reagent Co., Ltd. Silane coupling agent A-151 with a concentration of 99% was purchased from Shandong Shuntai New Materials Co., Ltd. 2,5-Dimethyl-2,5-di(*tert*-butylperoxy) hexane (DBPH) was purchased from Dongguan Aochuang Silicon Material Technology Co., Ltd. All reagents were used directly without undergoing secondary treatment.

2.2. Modification process of MWCNTs

Tannic acid (10 g) and MWCNTs (5 g) were dissolved in anhydrous ethanol (200 mL). The solution was stirred thoroughly and the beaker was shaken in an ultrasonic cleaner for 30 min. The passages were then washed several times repeatedly with ethanol and deionized water. Then, the cleaned

MWCNTs were dried in a vacuum oven for 24 h. Subsequently, 5 g of A-151 was dissolved in 100 mL of anhydrous ethanol solution, and the dried MWCNTs were co-mixed with the mixed solution and stirred using a magnetic stirrer for 12 h. The MWCNTs were then dried in the vacuum oven for 24 h.

2.3. Synthesis process of Ag@Cu powder

The Cu powder was mixed with anhydrous ethanol and deionized water to form a suspension (Cu concentration of 5 wt%) and then PVP was added and the suspension was magnetically stirred. AgNO₃ was mixed with deionized water to prepare Ag ion solution (the volume ratio of AgNO₃ to suspension is 1 : 1), and then the two were mixed and then slowly added to the glucose solution and stirred for 4 h. The reaction solution was then filtered under vacuum and washed repeatedly with deionized water and dried in a vacuum oven at 60 °C for 24 h. Finally, the dried Ag@Cu powder was heated in a vacuum oven at 200 °C for 2 h. 100 g of Ag@Cu and 10 g of A-151 were mixed and 50 mL of anhydrous ethanol solution was added. Then, it was magnetically stirred at 60 °C for 8 h. Finally, the mixture was dried in an oven at 60 °C for 24 h.

2.4. Preparation of the FVMQ/Ag@Cu/MWCNT composite

The present study employs a mechanical blending approach to fabricate the composite material. The FVMQ is plasticized in an open mill, followed by the addition of MWCNTs and the coupling agent A-151. Ag@Cu and DBPH are then added to the open mill. After the roll pitch was adjusted to 0.2 mm, the prepared mixture was placed in the open mill and passed through 5 times to ensure homogeneous mixing. Based on the vulcanization curve, the homogeneous material was placed in the mold and vulcanized at 160 °C and 10 MPa for 15 min. The samples were then placed in a vacuum oven at 170 °C for 10 min for secondary vulcanization to remove internal small molecule additives. The FVMQ for all sample formulations was 100 phr. For ease of reading, the samples were named C_xA_y, where *x* denotes the number of servings of MWCNTs and *y* denotes the number of servings of Ag@Cu powder.

2.5. Characterization

The microstructure of the sample was obtained using a scanning electron microscope (FE-SEM, JSM-7001F). Before the test, the sample was frozen and broken in liquid nitrogen and sputtered gold plating. The size distribution of particles in the composites from SEM images was analyzed using Nano Measure software. The mechanical properties of the material with a size of 10 × 10 × 2 mm were tested with a universal stretching machine, and the tensile speed was set to 500 mm min⁻¹. The crystal phases of materials were characterized by X-ray diffraction (Bruker, D8 ADVANCE XRD). The chemical structure was analyzed by Fourier transform infrared spectroscopy (FTIR, Nicolet 6700). The hardness of the material was tested using a Shaw hardness tester. The resistance of the material is measured with a four-probe tester (RTS-8). The CASS test was carried out by using a comprehensive environmental coupling test box, and the salt spray composition was 5 wt% NaCl and 0.26 g L⁻¹ CuCl₂, and pH = 3.1–3.3.

A UV aging test chamber (LRHS-NZY) is used to conduct UV aging experimental tests on materials, and the UV lamp type was UVA-340 with an irradiation intensity of $1.55 \pm 0.02 \text{ W m}^{-2} \text{ nm}^{-1}$ and a drying time of 8 h and a wetting time of 4 h. The constant temperature and humidity (HTHH) test chamber (LRHS-101-LH) is used to conduct HTHH experimental tests on materials, and temperature 60 °C and humidity 95% RH for 16 h; temperature 30 °C and humidity 95% RH for 8 h. By using a network vector analyzer (N5222B) to measure the scattering parameters (S_{11} , S_{12} , S_{21} , and S_{22}) of the material in the X-band (8.2–12.4 GHz frequency range), the EMI SE of the material in this frequency range can be calculated.

3. Results and discussion

After exposure to a salt solution, the potential difference between the different metals can easily induce an electrochemical reaction between the VMQ matrix and conductive metal fillers. This leads to the corrosion of rubber products and reduces the EMI shielding effectiveness of the conductive rubber. Currently, rubber matrix composites are required to exhibit intelligent responses to various environmental stimuli, including salt spray resistance, high temperature and humidity, UV aging resistance, and thermal management. For the first time, we propose a multiple-scale interface strategy to tightly integrate the rubber matrix with the conductive metal fillers, forming a stable FVMQ-based composite (Fig. 1). To overcome the inherent electrostatic repulsion and interface incompatibility between Ag@Cu nanoparticles, their molecular functionalization and surface environment were modified using an A-151 coupling agent. This modification enhanced the interaction between the Ag@Cu nanoparticles and the silicone rubber interface. Additionally, the introduction of MWCNTs further enhances both the electrical conductivity of the rubber product and the crosslinking degree of the FVMQ matrix. This also reduces the density of the FVMQ-based composite, meeting lightweight application requirements. The presence of A-151

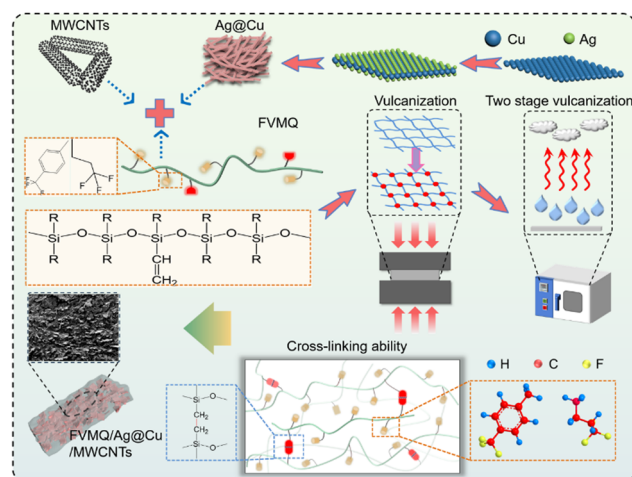


Fig. 1 Preparation flow chart of the FVMQ/Ag@Cu/MWCNT composites.

characteristic peaks can also be clearly observed by FTIR patterns of modified Ag@Cu and MWCNTs (Fig. S12, ESI[†]). The results of the modification were further verified.

In summary, the manufacturing process of FVMQ-based composites involves the preparation of core-shell Ag@Cu microspheres *via* chemical synthesis. Subsequently, modified Ag@Cu microspheres were obtained through A-151 coupling agent modification, which promoted interfacial electrostatic attraction and chemical interactions between different nanostructures. Finally, FVMQ-based products with multiple interface interactions (including dipole-dipole, electrostatic and chemical bonding) and stable, controllable properties were obtained through mechanical blending and vulcanization treatment.

Fig. 2 presents SEM images of the cross-sections of the samples, with Fig. 2(a–f) illustrating the microstructural characteristics of samples containing varying concentrations of the Ag@Cu filler. The prepared Ag@Cu flakes were tested by SEM and EDS (Fig. S10 and S11, ESI[†]), and from the SEM images, it can be seen that the flakes are Ag layers wrapped around the surface of the Cu core with a clear delamination. It is also clearly observed from the EDS image that the Ag layer is deposited on the surface of the Cu core. Fig. 2a depicts the cross-section of C10A0, which exhibits a smooth and even surface only in the presence of MWCNTs, indicating that the rubber matrix dominates the structure. Fig. 2(b–f) showcase samples with increasing concentrations of the Ag@Cu powder. In Fig. 2(b and c), when the content of the Ag@Cu filler is relatively low, the distribution of Ag@Cu particles within the rubber matrix is heterogeneous, with observable Ag@Cu particles limited to specific regions. At this stage, a complete

conductive pathway has yet to be established within the rubber matrix. As the Ag@Cu content increases, the material density rises, leading to tighter interconnections between Ag@Cu layers. In Fig. 2e, when the addition of the Ag@Cu powder reaches 200 phr, the powder forms a regular and dense layered structure within the rubber matrix. This stratified distribution interacts synergistically with MWCNTs, establishing a compact conductive network that enhances the electrical conductivity of the rubber and plays a critical role in improving the material's EMI SE value.^{36,37} However, further increases in the Ag@Cu loading result in the Ag@Cu particles dominating the spatial configuration (Fig. 2f). Excessive filler loading can exceed the filler limit of FVMQ, compromising the structural integrity of the rubber and disrupting the tight molecular chain arrangement after vulcanization. Additionally, an increased filler content leads to significant agglomeration of the Ag@Cu particles within the rubber matrix, resulting in defects in the vulcanized rubber, uneven stress distribution, and degradation of the material's mechanical properties. Fig. 2(g–i) shows the elemental mapping of C10A200, confirming the uniform distribution of Ag@Cu powder within the rubber matrix.

Fig. 3a presents the XRD characterization of Ag@Cu powder, where the peaks at $2\theta = 43.3^\circ$, 50.5° , and 74.1° correspond to the characteristic peaks (111), (200), and (220) of Cu, while the peaks at $2\theta = 38.1^\circ$, 44.27° , 64.4° , and 77.4° correspond to the characteristic peaks (111), (200), (220), and (311) of Ag.³⁸ The conductivity of the material is closely related to its EMI SE. Generally, higher conductivity correlates with superior EMI shielding performance. To investigate this relationship, we examined the influence of the Ag@Cu powder content on the conductivity of the samples. As shown in Fig. 3b, when only MWCNTs are present in the FVMQ matrix, the conductivity is

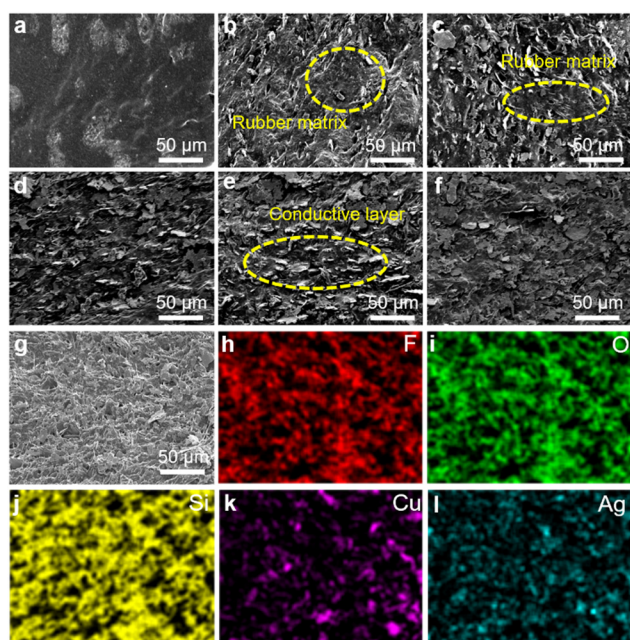


Fig. 2 SEM images of the different samples (a) C10A0, (b) C10A50, (c) C10A100, (d) C10A150, (e) C10A200, and (f) C10A250. (g)–(l) Elemental mapping images of C10A200.

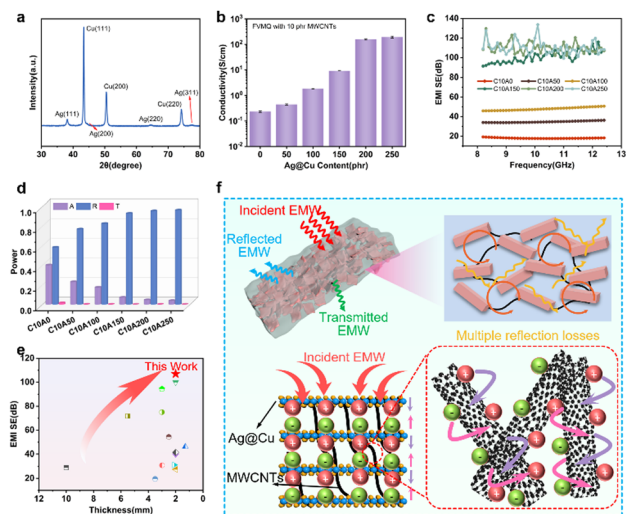


Fig. 3 (a) XRD characterization of Ag@Cu, (b) electrical conductivity of the different samples, (c) EMI SE of the different samples, (d) absorption coefficient (A), reflection coefficient (R) and transmission coefficient (T) of the different samples, (e) comparison of research efforts in related fields, and the (f) schematic diagram of the EMI shielding mechanism of composite materials.

relatively low (0.23 S cm^{-1}). Upon introducing Ag@Cu conductive metal powder, the increase in conductivity is initially insignificant due to insufficient dispersion of the powder within the rubber matrix, which prevents the formation of a dense and effective conductive network at low Ag@Cu concentrations. This observation is consistent with the microstructural analysis of the sample's cross-section (Fig. 2). When the Ag@Cu content reaches 200 phr, the conductivity increases dramatically to 155.16 S cm^{-1} , significantly surpassing that of C10A150.

According to percolation theory,^{39–41} when the filler content reaches the material's percolation threshold, a slight increase in the filler concentration results in a significant enhancement of electrical conductivity. Specifically, when FVMQ and Ag@Cu powders are mixed, the powder particles are irregularly distributed within the rubber matrix. However, once the added amount reaches a critical value, the metal particles approach each other and form interconnected regions within the rubber matrix, leading to percolation.^{42,43} Assuming the volume fraction of the filler is P and the percolation threshold is P_c , the electrical conductivity of the composite material exhibits a minimal variation with an increasing filler volume fraction when $0 < P < P_c$. Once the volume fraction reaches $P = P_c$, there is a substantial surge in the electrical conductivity of the composite. When $P > P_c$, the electrical conductivity tends to change more gradually.^{28,44} Using a network vector analyzer, the scattering parameters of the sample can be obtained, allowing the deduction of the material's EMI SE. Besides conductivity, another critical factor influencing the EMI shielding performance is the material thickness.^{45,46} To eliminate interference from the sample thickness on the EMI SE, this experiment employs a mold with a thickness of 2 mm, ensuring that all samples maintain a consistent thickness within this range. The EMI SE of the samples is illustrated in Fig. 3c and Fig. S2 (ESI†). When the conductive filler consists solely of MWCNTs, the EMI SE of C10A0 reaches 20 dB, which aligns with the standards of commercial EMI shielding materials. When the Ag@Cu content reaches 150 phr, the EMI SE of C10A150 improves to 93 dB, significantly exceeding the standard for commercial EMI shielding materials and enhancing the EMI SE by 44 dB compared to C10A100. The presence of MWCNTs facilitates the formation of a robust conductive network within the rubber matrix. As the Ag@Cu content continues to rise, C10A200 achieves an EMI SE of 107 dB, surpassing that of C10A150. Furthermore, C10A250 demonstrates an EMI SE of 109 dB, showing only marginal improvement compared to C10A200.

The absorption effectiveness (SE_A), reflection effectiveness (SE_R), absorbed power coefficient (A) and reflected power coefficient (R) are critical parameters for analyzing the mechanisms of EMI shielding materials,^{47,48} which can be calculated using eqn (S1) and (S3)–(S5) (ESI†). The variations in A , R , SE_A , and SE_R for different samples are illustrated in Fig. 3d and Fig. S5(a–f) (ESI†). C10A0 exhibits relatively low conductivity, with both SE_A and SE_R values being comparatively low, indicating that the sample surface has limited capability to reflect or

absorb EM waves. It is not until the Ag@Cu content reaches 150 phr that a significant increase in conductivity is observed, leading to a substantial enhancement in the material's ability to reflect EM waves, with an SE_R value of 80 dB. As the Ag@Cu content increases, the conductive fillers form a three-dimensional network structure within the rubber matrix. The network structure formed by the stacking of such layers enhances the propagation path of EM waves, and the multiple reflections of EM waves in the network also improve the EMI shielding performance of the material.⁴⁹ Consequently, EM waves entering the sample undergo multiple reflections and scattering events, resulting in rapid attenuation and energy dissipation in other forms, thereby causing a gradual increase in SE_A . The SE_A value reflects the material's capacity to absorb EM waves that penetrate its interior; however, it does not directly describe the material's inherent ability to absorb incident EM waves.

Fig. 3d illustrates the variations in A and R for samples with differing Ag@Cu concentrations. The A and R values serve as indicators of the reflection and absorption characteristics of the EM wave energy. As the Ag@Cu content increases, the electrical conductivity of the samples also rises, significantly enhancing their ability to reflect EM waves. For instance, C10A250 exhibits an R value of 0.96, indicating that nearly all incident EM waves are reflected at the interface between the material and air. Although the three-dimensional structure of the film at this stage is relatively dense, leading to a high specific SE_A value, the reflection of EM waves at the material's surface prevents them from effectively penetrating the material, thereby limiting their absorption. The T -value of C10A250 is essentially 0, indicating that EM waves cannot penetrate the material, demonstrating its excellent EM shielding capability. As the Ag@Cu content increases, the R value approaches 1 while the A value decreases toward 0. The shielding mechanism of the EMI shielding material can be assessed through the relationship between R and A values. Specifically, when the R value exceeds the A value, the material predominantly reflects EM waves. Fig. 3f presents a schematic diagram of the EM wave shielding process: part of the incident EM waves on the material surface are reflected, while the EM waves entering the material are attenuated in the form of heat through multiple reflections, with only a small portion passing through the material into the environment.⁵⁰ Fig. 3e compares the performance of this work with existing FVMQ-based EMI shielding composites, highlighting the significant advantages of the developed material.

The mechanical properties of FVMQ-based composites are critical to their stability and potential application scenarios. Fig. 4(a and b) demonstrates the folding and twisting tests of the samples, indicating that the samples retain the excellent flexibility characteristic of rubber even after undergoing significant deformations. Fig. 4c presents the vulcanization curves of the different samples, providing insights into the time required for complete vulcanization of the rubber. During the vulcanization process, the unsaturated bonds in the polymer chains of the rubber open, enabling the molecular chains to

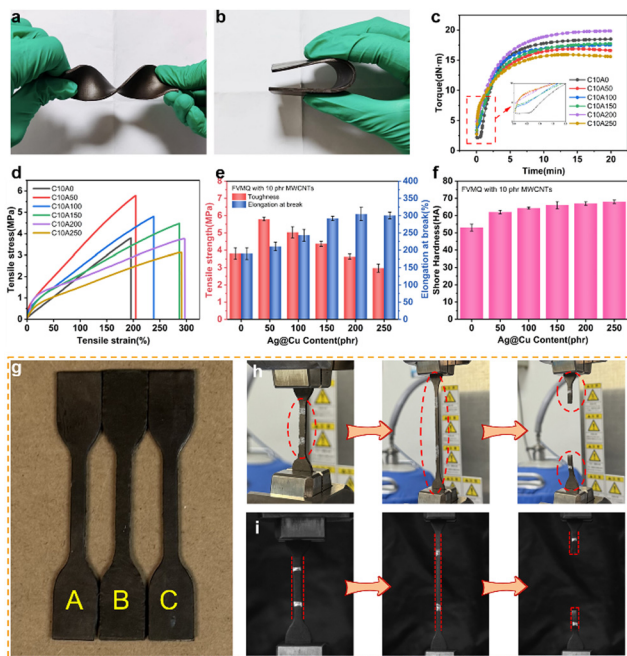


Fig. 4 (a) and (b) Twisting and bending of the samples, (c) vulcanization curves of the samples, (d) and (e) tensile strength and elongation at break of the samples, (f) shore hardness of the samples, and the (g)–(i) actual tensile process of the samples.

connect through these bonds. This transformation converts the rubber from a linear molecular structure into a three-dimensional network structure, significantly enhancing its mechanical properties. Fig. 4(d and e) illustrate the variations in the elasticity and toughness of different materials. As the Ag@Cu content increases, the tensile strength initially rises sharply and then gradually declines, while the elongation at break initially increases slowly and then decreases. When the Ag@Cu content reaches 50 phr, the tensile strength of the material increases from 3.8 MPa to 5.8 MPa. The interaction between Ag@Cu powders and MWCNTs maximizes the reinforcing effect of the fillers on FVMQ. Ag@Cu particles penetrate into the gaps between MWCNTs and interact with them within the rubber matrix, forming a more stable structure that further enhances the reinforcing effect of MWCNTs.

When the Ag@Cu content reaches 200 phr, the tensile strength of C10A200 matches that of C10A0, at 3.8 MPa. At this stage, the material retains the inherent high elasticity of rubber while exhibiting excellent EMI shielding performance. However, for C10A250, the predominance of the metal powder leads to uneven distribution and significant aggregation within the rubber matrix, resulting in numerous defects and a consequent loss in mechanical properties. As the Ag@Cu content continues to increase, the elongation at break reaches a maximum value of 306% at 200 phr. Beyond this point, the elongation at break starts to decrease. The introduction of Ag@Cu contributes to an initial increase in elongation at break because the increased filler content during vulcanization reduces the crosslink density of the rubber, thereby enhancing elongation. However, when the filler content exceeds the rubber's filler-loading limit,

the elongation at break decreases due to the formation of structural defects. Fig. 4f shows the changes in the hardness of the samples after the addition of Ag@Cu. The hardness of C10A50 significantly increases compared to the sample without Ag@Cu. Fig. 4(g–i) depict the tensile process of the material, where the fracture surfaces are smooth and located at the center of the tensile strip. This observation further confirms the uniform distribution of fillers within the material.

The incorporation of MWCNTs into the FVMQ matrix provides a significant reinforcing effect. The macromolecular chains in the rubber adsorb onto the filler surface, while shorter molecular chains slide along the adsorbed surface rather than breaking directly during tensile deformation (Fig. 5g). In this case, the stress is primarily borne by longer linear chains, reducing the stress concentration and thereby enhancing the strength of the rubber. However, the plastic deformation of the material is limited due to the restricted mobility of individual MWCNTs within the surrounding matrix chains. Excessive addition of MWCNTs can lead to a reduction in rubber elasticity. Therefore, determining an optimal filler content that maximizes the strength of the rubber while minimizing the loss of elasticity is critical. Based on the comprehensive performance of the samples, we found that sample C10A200 exhibits superior EMI SE when the Ag@Cu content is 200 phr. Additionally, C8A200 retains the flexibility characteristic of polymer materials. Fig. 5a compares the EMI SE of samples C0A200 and C10A200, both initially and after being exposed to a natural environment for 60 days. The results reveal that C0A200 demonstrates a slightly lower EMI SE than C10A200. This finding further highlights the critical role of MWCNTs in constructing continuous conductive pathways

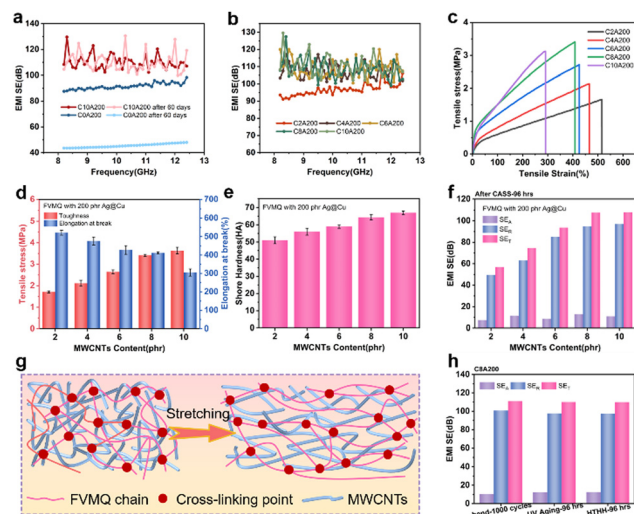


Fig. 5 (a) EMI SE of C10A200 and C0A200 after 60 days of placement in natural environments, (b) EMI SE of the different samples, (c) and (d) tensile strength and elongation at break of different samples, (e) shore hardness of the different samples after the CASS test, (f) EMI SE of the different samples after the CASS test, (g) schematic diagram of the reinforcing effect of MWCNTs inside the rubber matrix, and the (h) EMI SE after C8A200 simulated special environmental corrosion.

within the rubber matrix. Moreover, the EMI SE of C10A200 remains virtually unchanged after 60 days of exposure to natural environments, while the EMI SE of C0A200 drops significantly from 88 dB to 55 dB. This indicates that the introduction of MWCNTs enhances the material's resistance to environmental degradation, thereby preserving its performance over time. The addition of MWCNTs significantly influences the mechanical properties of FVMQ, and excessive filler content can adversely affect its elasticity.

To investigate the environmental corrosion resistance of the material, we fixed the Ag@Cu content and varied the MWCNT content. Fig. 5b and Fig. S3 (ESI[†]) display the EMI SE of samples with different MWCNT contents. As the MWCNT content increases, more complete conductive pathways are established within the rubber matrix. Fig. 5(c and d) shows that MWCNTs exhibit a significant reinforcing effect on the rubber, with the tensile strength of the samples steadily increasing as their content rises, from 0.43 MPa to 3.41 MPa. This indicates a positive correlation between the tensile strength and the MWCNT content. While MWCNTs effectively reinforce the FVMQ matrix, excessive addition can lead to a partial loss of elasticity in the rubber material. Fig. 5e illustrates the effect of the MWCNT content on the hardness of the samples, showing a significant increase in the hardness with a higher MWCNT content.

To investigate the effect of MWCNTs on the environmental corrosion resistance of the samples, we performed CASS tests on different samples. With a small amount of MWCNTs introduced, the EMI SE of the samples still showed a notable decline after corrosion. However, when the MWCNT content reached 6 phr, sample C6A200 exhibited only a slight decrease in EMI SE after 96 h of corrosion (Fig. 5f). In contrast, the EMI SE of C8A200 remains unchanged after corrosion and exhibits excellent corrosion resistance. This improvement can be attributed to the introduction of MWCNTs, which increase the cross-link density of the rubber material and promote tighter bonding between molecular chains. Consequently, the volatilization of small molecules in rubber does not produce obvious vacancies or defective spots within the FVMQ matrix, and it is difficult for moisture or small molecules in the environment to penetrate and remain inside the rubber. This prevents internal filler corrosion and maintains the material's integrity. Fig. 5h presents the EMI SE of sample C8A200 after 1000 bending cycles, 96 h of UV aging, and 96 h of HTHH testing. Even after exposure to external mechanical bending and harsh environmental conditions, the material retains a high level of EMI SE. This composite material not only exhibits excellent EMI SE but also demonstrates superior flexibility and outstanding resistance to environmental corrosion. These properties enable conductive polymer composites to maintain long-term durability in complex operating environments, making them highly suitable for advanced applications.

Fig. 6a presents the water contact angles on the surfaces of various samples. The incorporation of MWCNTs progressively enhances the hydrophobicity of the material's surface, achieving a maximum water contact angle of 112°. When the material

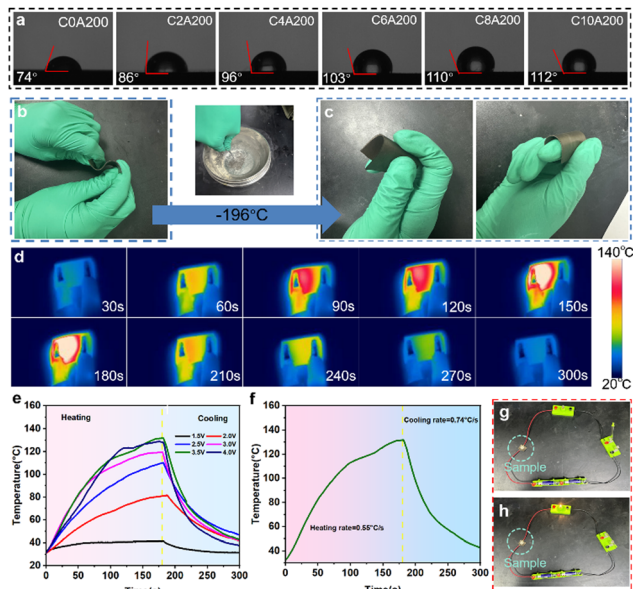


Fig. 6 (a) Water contact angle of the material surface second, (b) and (c) appearance change of the material before and after a low-temperature environment, (d) infrared thermography of the material during warming up and cooling down, (e) and (f) sample warming and cooling curves, and (g) and (h) conductivity verification of C8A200 after the CASS test.

surface exhibits significant hydrophobic characteristics, it effectively prevents moisture from penetrating directly into the FVMQ matrix, thereby reducing the likelihood of water or other small molecules remaining within the rubber substrate and causing corrosion to the metal powder. Fig. 6(b and c) demonstrate the self-recovery capability of the material at cryogenic temperatures. When sample C8A200 is immersed in liquid nitrogen at -196°C , it undergoes rapid freezing but promptly returns to its original state upon removal. The tests for the material's delamination resistance and scratch resistance are shown in Fig. S8 and S9 (ESI[†]). We applied commercial transparent tape to the surface of the sample and rapidly peeled it off, observing no adhesion of the powder filler to the tape. Additionally, we conducted a manual abrasion test on the sample surface using our fingers and found no evidence of scratches, fractures, or powder detachment. This can be attributed to the strong bonding between the powder and the FVMQ matrix during the vulcanization process.

Fig. 6(d–f) demonstrate the material's warming and cooling processes under different applied voltages. When a voltage of 3.5 V is applied across the sample, it rapidly heats up and maintains a temperature above 130°C (Fig. 6f). Upon power disconnection, the sample quickly cools to room temperature. These results indicate that the prepared composites exhibit excellent electrically driven thermal response, making them highly promising for thermal management applications.^{51,52} This process further confirms the material's favorable thermoelectric effect. Fig. 6(g and h) validate the electrical conductivity of sample C8A200 after CASS testing (Fig. S7, ESI[†]). When sample C8A200 is integrated into the circuit shown in the figure, the lamp illuminates upon closing the circuit breaker,

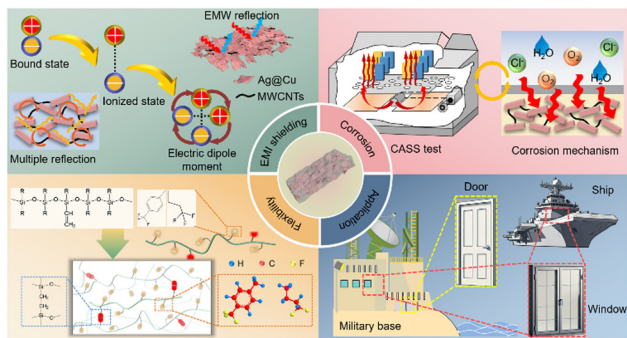


Fig. 7 EMI shielding mechanism of the composites, the simulated corrosion effect of the composites in marine environments, highly flexible mechanical interlocking strategy of the composites and practical application scenarios of the composites.

indicating that the material forms a conductive pathway. This observation verifies that the material retains its excellent electrical conductivity post-CASS testing, demonstrating robust conductive capabilities. The FVMQ/Ag@Cu/MWCNT composites developed in this work can effectively shield EM waves. Fig. 7 illustrates the EMI shielding mechanism of this composite material, the simulated corrosion effect of the material in the marine environment, the mechanical interlocking strategy enabling high flexibility, and practical application scenarios. These composites are suitable for use in harsh marine environments, such as climate-controlled military bases, ship windows, and door gaps for sealing packages.^{53,54} This study provides new insights into the development of flexible shielding materials with enhanced environmental corrosion resistance.

4. Conclusions

We successfully synthesized EMI shielding composites with exceptional environmental durability and high efficiency *via* mechanical blending. By utilizing FVMQ as the matrix, we constructed a conductive three-dimensional network within the rubber matrix through the incorporation of MWCNTs and conductive metal powders such as Ag@Cu. This approach not only imparted conductivity to FVMQ but also endowed it with outstanding EMI shielding capabilities, achieving an EMI SE exceeding 100 dB while preserving the inherent high flexibility of the rubber material. Furthermore, the introduction of MWCNTs enhanced the crosslinking density of the rubber, enabling the samples to retain high EMI SE even after undergoing rigorous tests such as the CASS test, UV aging test, and HTHH test. Notably, after 1000 bending cycles, the EMI SE of sample C8A200 exhibited no significant decline, consistently demonstrating stable performance. Additionally, the material's surface displayed excellent hydrophobic properties, effectively preventing moisture from penetrating the rubber matrix and corroding the metal powder fillers. Future research should focus on further exploring the design and application of novel corrosion-resistant metal fillers (*e.g.*, graphene-coated metals, high-entropy alloys, *etc.*). Moreover, integrating multi-scale

simulations with *in situ* characterization techniques is essential for comprehensively elucidating the degradation mechanisms of composite materials under EM-chemical coupling conditions. Such an approach will provide robust theoretical support for designing the next generation of EMI materials, which possess both high shielding efficiency and excellent environmental stability.

Author contributions

Jiahao Sun: writing – original draft and investigation. Lijian Mao: methodology. Zhenliang Gao: methodology and conceptualization. Lechun Deng: methodology and conceptualization. Qiang Chen: supervision and project administration. Yang Li: writing – review & editing, project administration, and conceptualization. Chuntai Liu: supervision and project administration. Changyu Shen: supervision and project administration. Xianhu Liu: supervision, project administration, and funding acquisition.

Conflicts of interest

There are no conflicts to declare.

Data availability

The data supporting this article have been included as part of the ESI.†

Acknowledgements

This project was supported by the Natural Science Foundation of Henan (242300421010).

References

- 1 Y. Zhang, S. D. Yang, Q. Zhang, Z. Y. Ma, Y. J. Guo, M. Shi, H. Wu and S. Y. Guo, *Carbon*, 2023, **206**, 37–44.
- 2 T. Zhou, D. H. Zhang, K. L. Diao, J. J. Du, Y. P. Hu, Z. Lei, D. J. Liu, S. Liu and S. H. Qin, *Mater. Today Nano*, 2025, **29**, 100606.
- 3 Y. Zhang, H. Wu and S. Y. Guo, *ACS Appl. Mater. Interfaces*, 2022, **14**, 40351–40360.
- 4 X. Zhang, J. L. Chen, X. Z. Chen, J. H. Yao, W. G. Zheng and B. Shen, *Chem. Eng. J.*, 2024, **493**, 152478.
- 5 S. Zhang, C. J. Wang, T. H. Gao, J. R. Hu, P. J. Lu, B. J. Guo, Q. F. Xu, K. Liu, B. W. Li, R. Tu, M. J. Yang and K. Ando, *ACS Appl. Mater. Interfaces*, 2023, **15**, 15965–15975.
- 6 L. Zhang, X. X. Ding, D. B. Lin, Y. B. Feng, H. L. Fu, G. Xiao, P. Xu and Q. L. Li, *Composites, Part B*, 2025, **297**, 112339.
- 7 T. Yun, H. Kim, A. Iqbal, Y. S. Cho, G. S. Lee, M. K. Kim, S. J. Kim, D. Kim, Y. Gogotsi, S. O. Kim and C. M. Koo, *Adv. Mater.*, 2020, **32**, 1906769.
- 8 J. F. Wang, X. X. Jin, H. Wu and S. Y. Guo, *Carbon*, 2017, **123**, 502–513.

- 9 J. M. Yang, X. Liao, G. Wang, J. Chen, F. M. Guo, W. Y. Tang, W. Wang, Z. H. Yan and G. X. Li, *Chem. Eng. J.*, 2020, **390**, 124589.
- 10 L. L. Xing, H. R. Cheng, Y. Li, Q. Chen and X. H. Liu, *Chem. Eng. J.*, 2024, **487**, 150729.
- 11 L. L. Xing, H. R. Cheng, Y. Li, Q. Chen, C. T. Liu, C. Y. Shen and X. H. Liu, *Small*, 2025, **21**, 2407337.
- 12 Z. J. Wei, Y. Cheng, Y. R. Sun, Y. H. Zhan, Y. Y. Meng, Y. C. Li, H. S. Xia and X. C. Jiang, *Compos. Sci. Technol.*, 2025, **259**, 110960.
- 13 J. S. Wei, P. He, Y. T. Yang, C. X. Tang, Z. Long, X. Chen, T. Z. Lei and L. Dai, *Chem. Eng. J.*, 2024, **497**, 154969.
- 14 Q. H. Wang, J. Zhang, Z. H. Zhou, J. Q. Zhao, Y. Yi, S. Y. Feng, Z. Y. Sui, W. Zhang and C. H. Lu, *Small*, 2024, **20**, 2309803.
- 15 Q. Wang, S. M. Liu, S. Q. Liu, Z. Zuo, Y. F. Gao, C. Wu and X. D. Liang, *Nano Today*, 2024, **58**, 102406.
- 16 G. Wang, X. Liao, J. M. Yang, W. Y. Tang, Y. Zhang, Q. Y. Jiang and G. X. Li, *Compos. Sci. Technol.*, 2019, **184**, 107847.
- 17 Y. B. Tian, X. Z. Feng, J. Wang, S. B. Shang, F. Liu, J. X. Jiang, H. B. Zhang, Y. X. Chen and Z. Q. Song, *Chem. Eng. J.*, 2025, **508**, 161065.
- 18 W. Sun, Z. C. Lou, L. Xu, Q. L. Ma, H. Han, M. L. Chen, Q. Y. Wang, J. Q. Han and Y. J. Li, *Chin. J. Polym. Sci.*, 2024, **42**, 864–873.
- 19 Y. Chen, X. M. Shao, L. He, Y. N. Xu, Q. Y. Yao, D. Feng and W. C. Wang, *Chin. J. Polym. Sci.*, 2024, **42**, 864–873.
- 20 Y. Li, Y. C. Qing, Y. R. Zhang and H. L. Xu, *J. Adv. Ceram.*, 2023, **12**, 1946–1960.
- 21 Y. Li, Y. C. Qing, H. Y. Yao, H. L. Xu and H. J. Wu, *J. Colloid Interface Sci.*, 2023, **645**, 165–175.
- 22 L. C. Deng, Z. W. Wang, J. Z. Wu, X. S. Gu, H. Yu, Y. Li, Y. R. Cao, F. Luo, X. H. Liu and Q. Chen, *Compos. Sci. Technol.*, 2025, **259**, 110937.
- 23 J. N. Su, Q. Y. Li, W. Tan, Q. Jiang, L. Li and J. G. Ju, *Appl. Mater. Today*, 2025, **42**, 102565.
- 24 F. Y. Hu, F. Zhang, X. H. Wang, Y. Y. Li, H. L. Wang, R. Zhang, H. X. Li and B. B. Fan, *J. Adv. Ceram.*, 2022, **11**, 1466–1478.
- 25 Y. Qiao, Y. Wang, J. Yang, Q. Li and J. Gu, *Composites, Part A*, 2023, **172**, 107618.
- 26 L. C. Deng, K. Yang, W. Z. Wang, W. J. Zhang, Y. Li, H. Y. Nan, X. Chai, F. Luo, H. J. Wu and Q. Chen, *J. Mater. Sci. Technol.*, 2025, **224**, 292–301.
- 27 T. Chen, J. Cai, D. Gong, X. Cheng, P. Liu and D. Y. Zhang, *J. Mater. Chem. C*, 2023, **11**, 6597–6606.
- 28 S. Kwon, R. Ma, U. Kim, H. R. Choi and S. Baik, *Carbon*, 2014, **68**, 118–124.
- 29 T. Mai, W. Y. Guo, P. L. Wang, L. Chen, M. Y. Qi, Q. Liu, Y. Ding and M. G. Ma, *Chem. Eng. J.*, 2023, **464**, 142517.
- 30 X. F. Ma, J. J. Pan, H. T. Guo, J. W. Wang, C. M. Zhang, J. Q. Han, Z. C. Lou, C. X. Ma, S. H. Jiang and K. Zhang, *Adv. Funct. Mater.*, 2023, **33**, 2213431.
- 31 W. J. Ma, W. R. Cai, W. H. Chen, P. J. Liu, J. F. Wang and Z. X. Liu, *Chem. Eng. J.*, 2021, **426**, 130729.
- 32 Z. Liu, X. Gao, B. Zhu and X. Yuan, *Chem. Eng. J.*, 2024, **495**, 153528.
- 33 Y. J. Liu, J. T. Zhou, Z. L. Ning, H. X. Huang, Z. Y. Cheng, L. T. Duan, Y. C. Wang, X. W. Tao, P. J. Liu, Y. Ma and Z. J. Yao, *Adv. Funct. Mater.*, 2024, **34**, 2411573.
- 34 L. X. Liu, W. Chen, H. B. Zhang, Q. W. Wang, F. L. Guan and Z. Z. Yu, *Adv. Funct. Mater.*, 2019, **29**, 1905197.
- 35 Y. Li, Y. C. Qing, Y. R. Cao, F. Luo and H. J. Wu, *Small*, 2023, **19**, 2302769.
- 36 J. Liu, H. B. Zhang, R. H. Sun, Y. F. Liu, Z. S. Liu, A. G. Zhou and Z. Z. Yu, *Adv. Mater.*, 2017, **29**, 1702367.
- 37 Z. Y. Li, Y. Sun, B. Zhou, Y. Z. Feng, C. T. Liu and C. Y. Shen, *Mater. Today Phys.*, 2023, **32**, 101017.
- 38 T. Rasouli, M. Pourabdoli, V. A. Lashgari and A. G. Hamidi, *Transit. Metal. Chem.*, 2024, **49**, 343–354.
- 39 Y. K. Li, M. X. Liu, C. Y. Li, K. P. Cui, L. B. Li and L. C. Jia, *Composites, Part B*, 2025, **296**, 112269.
- 40 W. W. Li, H. Jin, Z. H. Zeng, L. P. Zhang, H. Zhang and Z. Zhang, *Carbon*, 2017, **121**, 544–551.
- 41 S. Y. Li, Y. K. Du, H. R. Ye, J. M. Wu, Y. Wang, Y. Y. Liang, M. W. Zhu, S. S. Lam, C. W. Liu, J. Z. Li and C. L. Xia, *Adv. Funct. Mater.*, 2024, **34**, 2406282.
- 42 J. C. Li, X. Y. Zhao, W. J. Wu, X. W. Ji, Y. L. Lu and L. Q. Zhang, *Chem. Eng. J.*, 2021, **415**, 129054.
- 43 G. S. Lee, T. Yun, H. Kim, I. H. Kim, J. Choi, S. H. Lee, H. J. Lee, H. S. Hwang, J. G. Kim, D. W. Kim, H. M. Lee, C. M. Koo and S. O. Kim, *ACS Nano*, 2020, **14**, 11722–11732.
- 44 T. Kaneko, S. Ito, T. Minakawa, N. Hirai and Y. Ohki, *Polym. Degrad. Stab.*, 2019, **168**, 108936.
- 45 L. C. Jia, C. G. Zhou, W. J. Sun, L. Xu, D. X. Yan and Z. M. Li, *Chem. Eng. J.*, 2020, **384**, 123368.
- 46 A. Ghaffarkhah, S. A. Hashemi, S. Rostami, M. Amini, F. Ahmadijokani, A. P. Isfahani, S. E. Mhatre, O. J. Rojas, M. Kamkar, S. Wuttke, M. Soroush and M. Arjmand, *Adv. Funct. Mater.*, 2023, **33**, 2304748.
- 47 Y. J. Guo, Y. Zhang, H. Wu and S. Y. Guo, *J. Mater. Sci. Technol.*, 2024, **190**, 24–32.
- 48 Z. H. Fu, Y. F. Wu, Y. Z. Li, K. Huang, Q. S. Li, H. M. Yao, W. T. Cao, S. Gao, Y. Qin, Z. C. Zheng, J. C. Xu, M. Lei, K. Bi and H. Wu, *J. Materiomics*, 2025, **11**, 100936.
- 49 X. H. Wang, S. Bao, F. Y. Hu, S. Y. Shang, Y. Q. Chen, N. Zhao, R. Zhang, B. Zhao and B. B. Fan, *Ceram. Int.*, 2022, **48**, 16892–16900.
- 50 F. Y. Hu, H. F. Tang, F. S. Wu, P. Ding, P. G. Zhang, W. W. Sun, L. Z. Cai, B. B. Fan, R. Zhang and Z. M. Sun, *Small Methods*, 2024, **8**, 2301476.
- 51 Z. M. Fan, D. L. Wang, Y. Yuan, Y. S. Wang, Z. J. Cheng, Y. Y. Liu and Z. M. Xie, *Chem. Eng. J.*, 2020, **381**, 122696.
- 52 J. W. Dong, Y. Z. Feng, K. Lin, B. Zhou, F. M. Su and C. T. Liu, *Adv. Funct. Mater.*, 2024, **34**, 2310774.
- 53 K. P. Ruan, X. T. Shi, Y. L. Zhang, Y. Q. Guo, X. Zhong and J. W. Gu, *Angew. Chem., Int. Ed.*, 2023, **62**, e202309010.
- 54 F. Y. Hu, X. H. Wang, S. Bao, L. M. Song, S. Zhang, H. H. Niu, B. B. Fan, R. Zhang and H. X. Li, *Chem. Eng. J.*, 2022, **440**, 135855.